Durham University

Physics Department

MPhys F301

Outer Profiles of S0 Galaxies in the Coma Cluster

Author:
Shaun Read

Supervisor:
Dr. John Lucey

Submitted: 30 April 2014

ABSTRACT

This study uses i-band imagery from both the Tenth Data Release of the Sloan Digital Sky Survey (SDSS DR10) and the latest MegaCam release to study truncated lenticular (S0) galaxies in the Coma cluster. Using an image from each camera we take two 1D profiles along the major axis of each. We develop algorithms for measuring sky, finding the break point and characterising the truncation for use with the 1D profiles. Using a sample of known disk galaxies, we refine the sample to include only 66 S0s with disk dominated outer disks and axis ratio $b/a > 0.4$. We find that 74^{+5}_{-5}% of S0s are anti-truncated and 24^{+6}_{-5}% exhibit a pure exponential. Comparing to previous work in the Virgo cluster. We agree that there is a negligible fraction of truncated/down-bended disks in the cluster environment. But we also measure no variation of type-I disks between field and Coma cluster environments. We observe a weak trend between truncated disk frequency and distance from cluster centre: 80^{+9}_{-7}% of disks at $R_{clust} < 68$ Mpc are anti-truncated as opposed to 60^{+14}_{-12}% at $R_{clust} > 68$ Mpc.

Contents

1 Introduction **2**

1.1 Galaxy Properties 3

1.2 S0s and Classification 4

1.3 Photometry 5

1.4 The Origins of S0 Galaxies 6

1.5 Truncation 7

1.6 Aims of Project 9

2 Data and Initial Sample **9**

3 Data Reduction and Analysis **9**

3.1 Extracting 1D Profiles 9

3.2 Sky Subtraction 10
3.2.1 The effects of sky 10
3.2.2 Finding the Sky 10
3.3 Bulge-Disc Decomposition 12
3.4 Truncation Detection 14
3.5 Parameter Uncertainties 16

4 Results **16**
4.1 Sky Detection 16
4.2 Example Decomposition 17
4.3 Sample Properties 19
4.4 Correlations 22

5 Discussion **23**
5.1 Problems with this method 24

6 Conclusion **25**

1. Introduction

Ever since the 1920 Great Debate on the nature of nebulae, it has been known that the Milky Way is not the entirety of our universe, that there are indeed other 'island universes' called galaxies (Berendzen et al. 1976).

Modern ideas on how these immense structures formed describe quantum fluctuations in the very early universe becoming stretched during the inflationary period (Liddle 2003). Significant gravitational perturbations arise out of these expanded wrinkles in space and after enough matter is accumulated star formation can begin (Coles 2002).

It is therefore important to understand the nature of galaxy formation if we wish to test cosmological models, since there is a direct relationship between large scale structure formation and cosmological parameters (Binney 1998).

The most popular cosmology currently in use, ΛCDM (Cold Dark Matter), correctly predicts the existence of the CMB (Cosmic Microwave Background), the distribution of galaxies and the abundances of light elements (Coles 2002). However, ΛCDM simulations diverge from observation at the galactic scale, predicting excessive numbers of dwarf galaxies (Silk & Nusser 2010) and too few massive bulgeless galaxies with thin disks (Kormendy et al. 2010).

Constraining galaxy properties with observation allows one to constrain or perhaps modify aspects of the ΛCDM and hence lead to a more certain understanding of the cosmological properties of the early universe.

1.1. Galaxy Properties

Galaxies are not all indistinct clumps of stars but can take on a range of diverse structures (Hubble 1926). Most galaxies can be crudely classified into three broad categories based on stellar content and morphology: Elliptical, Spiral and Irregular.

Ellipticals are centrally condensed objects with a typical diameter from under 1 kpc to 200 kpc (Carroll & Ostlie 2007) and a smooth almost featureless luminosity profile. Ellipticals, as their name suggests, exhibit an elliptical shape ranging from ellipticity $\epsilon = 1$ (spheroidal E0) to around $\epsilon = 0.7$ (very oblate E7). Ellipticals contain little gas and hence little ongoing star formation due to their low gravitational binding energy (Crocker et al. 2011). Because they contain mostly old stars, ellipticals have higher metallicity and are thoroughly within the red sequence, hence they are commonly called 'red and dead' (Binney & Merrifield 1998).

Fig. 1.— From left to right: Elliptical ESO-325-G004, Lenticular NGC7049 and Spiral NGC5457 the 'pinwheel'

Spirals, in contrast, are very different to ellipticals in their structure. They are blueish disk galaxies usually with a redder central bulge and spiral arms with vivid dust lanes (Sparke 2000). The spiral arms are in fact density perturbations travelling around the disk, where the the increase in gas density initiates local star formation (Kennicutt 1998). They therefore contain many more younger main sequence stars, typically giving spirals a bluer hue of $0.4 \lesssim B - V \lesssim 0.8$, where B and V are the magnitudes in the 'blue' and 'visible' wavebands in the UBV photometric system (Sparke 2000).

1.2. S0s and Classification

The traditional method of classifying galaxies is the Hubble Tuning Fork (Hubble 1926). Hubble arranged galaxies from 'early' to 'late' types with the implicit assumption that all galaxies evolved that way in time. We now know that this transformation from early to late type is impossible since there is no way for ellipticals to increase their negligible angular velocity to match that of fast rotating spirals (Carroll & Ostlie 2007).

Spirals are sorted by the bulge size and tightness of their spiral arms and ellipticals by their ellipticity. On this continuous fork, an intermediate 'lenticular' class is necessarily created. Lenticulars, or S0 galaxies, are observed to share the stellar content of ellipticals but

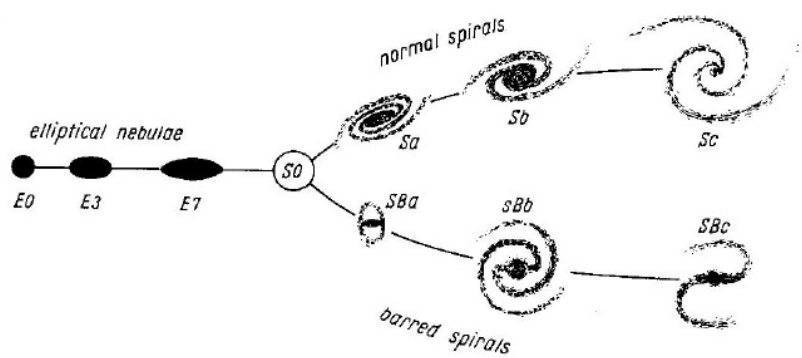

Fig. 2.— The Hubble Tuning Fork diagram. Early types are shown on the left with late types on the right (Hubble 1926)

the structure and kinematics of spirals. They are disk galaxies but have a smooth brightness profile free from spiral arms (Blanton & Moustakas 2009). S0s can be dusty and have few HII regions associated with young stars (DeGraaff et al. 2007). Together with a high metallicity, these properties give the galaxy a 'red and dead' appearance with $0.7 \lesssim B - V \lesssim 0.9$.

Due to their similarity with ellipticals, there have been many misclassifications of S0s

with low inclinations (side-on) (Laurikainen et al. 2005). S0s do not have significant emission on the Hα line and estimates of dynamical mass become challenging (Dressler & Sandage 1983). S0s have a central spheroidal component or bulge, which on average, is flatter than an elliptical, and unlike spiral bulges, iss usually brighter than its disk (Dressler 1980).

1.3. Photometry

Morphological classification remains, by its qualitative nature, subjective and open to interpretation (Naim et al. 1995). Using the quantitative measure of galaxy luminosity profiling minimises disagreement between observers and helps to quantify physical properties with more certainty.

Profiles are generated by isophotal analysis, whereby one fits thin ellipses of equal intensity (an 'isophote') to the image, working outwards from the previously established centroid. Plotting the average isophote intensity against geometric mean radius generates a 1D intensity profile (Peng et al. 2002). Now galaxy can be fitted by mathematical models and the resulting parameters analysed.

De Vaucouleurs was one of the first to propose his $R^{1/4}$ model for galaxy light distribution (de Vaucouleurs 1963). This model was successful in fitting elliptical galaxies and is still used today with bulges of S0 and spiral galaxies (Allen et al. 2006). However, this model does not describe all bulges well and an exponential model best describes disks! Given this variation in model parameters, the De Vaucouleurs model can be generalised to a Sérsic $R^{1/n}$ model (Sersic 1968).

$$I(R) = I_e \mathrm{exp}\left\{-\mathrm{b_n}\left[\left(\frac{\mathrm{R}}{\mathrm{R_e}}\right)^{1/\mathrm{n}} - 1\right]\right\}, \tag{1}$$

where $I(R)$ is the intensity at radius R, n is the Sersic index, R_e is the effective radius which encloses half the total intensity, I_e is the intensity at R_e and b_n is defined such that $\Gamma(2n) = 2\gamma(2n, b_n)$, where Γ is the complete gamma function and γ is the incomplete gamma function.

Figure 3 shows the effects of adjusting the Sérsic index with respect to a constant effective surface brightness. As n becomes smaller, the light becomes more centrally concentrated and lower in central intensity (Graham & Driver 2005).

Most galaxies do not consist purely of one component (Laurikainen et al. 2005), but include several, such as disks, bulges and bars (Rawle et al. 2013). The Sérsic model has been found to fit all of these components with small residuals and is reliably used to classify galaxies into morphological type (Peng et al. 2010).

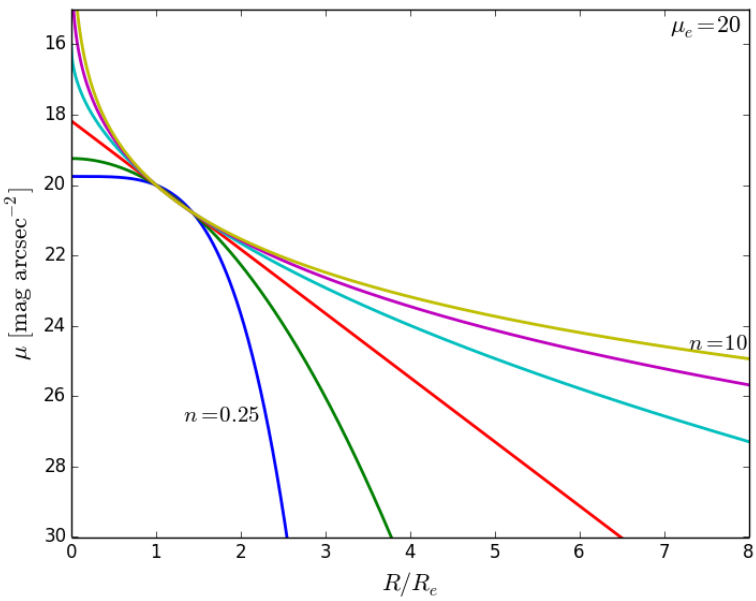

Fig. 3.— Magnitude profiles of Sersic indices from 0.25 to 10 with an effective magnitude of 20 mags

1.4. The Origins of S0 Galaxies

The origin of lenticular galaxies remains a highly active area of research. Logic dictates two possibilities for S0 formation: Either they formed in the same manner as ellipticals at the start of the galaxy formation era or they have since evolved from spirals by some unknown mechanism (Burstein et al. 2005).

If S0s did indeed transform from spiral-like galaxies, then a corresponding increase in the population of spirals should be seen over increasing redshift. This trend has been observed, showing an increase in early-types with look-back time (Dressler et al. 1997).

There is also evidence from the Tully-Fisher Relation (TFR), in which galaxy luminosity is related to maximum rotational velocity (Tully & Fisher 1977). This relation is tightly defined for local spirals, with small intrinsic scatter, as 0.43 ± 0.03 mag averaged over SDSS griz bands (Pizagno et al. 2007). Now that reliable TFRs have been constructed for S0s (Bedregal et al. 2006), the existence of an offset from spirals is confirmed. S0s are fainter than spirals by an average of 0.85 ± 0.19 mag in the i-band, with a similar offset found in the g and K_s bands (Rawle et al. 2013). This offset can be interpreted as the cessation of star formation and subsequent fading of the disk.

Various mechanisms for quenching star formation have been proposed. Ram-pressure

stripping removes the disk gas necessary for subsequent star formation (Gunn & Gott 1972); strangulation would remove larger reservoirs of halo gas, having a slower and gentler impact on star formation; or the harsher minor merger of two spirals, exhausting a large amount of the interstellar medium (ISM) (Bekki 1998) to name but a few.

The typical surface brightness of S0s has actually found to be greater than that of spirals (Burstein et al. 2005), and the bulge luminosity of S0s is too large to evolve from disk fading alone (Cortesi et al. 2013). The increased brightness favours minor mergers or galaxy harassment, where frequent high speed encounters strip disk gas and dump some of it at the centre (Moore et al. 1996).

The well-known morphology-density relation (Dressler 1980), describes an increase in early types with projected surface density. This is to be expected if S0s result from galaxy interactions, but S0s are observed in the field, suggesting that this may not be the whole story. If this is indeed the case, then either cluster based mechanisms such as ram-pressure stripping cannot be responsible for S0 formation, or there are multiple evolutionary paths to S0s operating in different environments.

If the evolutionary mechanism is dependent on density, then there may be structural differences in S0 galaxies as a function of environment which can be used to probe evolutionary history.

1.5. Truncation

One feature, suitably sensitive to external interactions, is the outer structure of the disk (Pohlen et al. 2004). The outermost radii should be vulnerable to the effects of galaxy-galaxy interactions, late-time accretion and gas stripping, hence retaining an imprint of the formation process.

Disk galaxies have been known not to obey an infinitely extended exponential light distribution for 35 years (van der Kruit 1979). It has become apparent that most -79% according to Pohlen et al. (2001)- disk galaxies exhibit ‘truncations’ or ‘breaks’ in their otherwise smooth exponential profiles.

S0 galaxy truncations can fall into three broad truncation classes: Type-I: single-exponential, Type-II: classically truncated (Freeman 1970) or Type-III: anti-truncated (Erwin et al. 2005).

Though early analysis indicated an even distribution of types in local S0s (Gutiérrez et al. 2011), when the cluster and field are analysed separately a distinct difference arises.

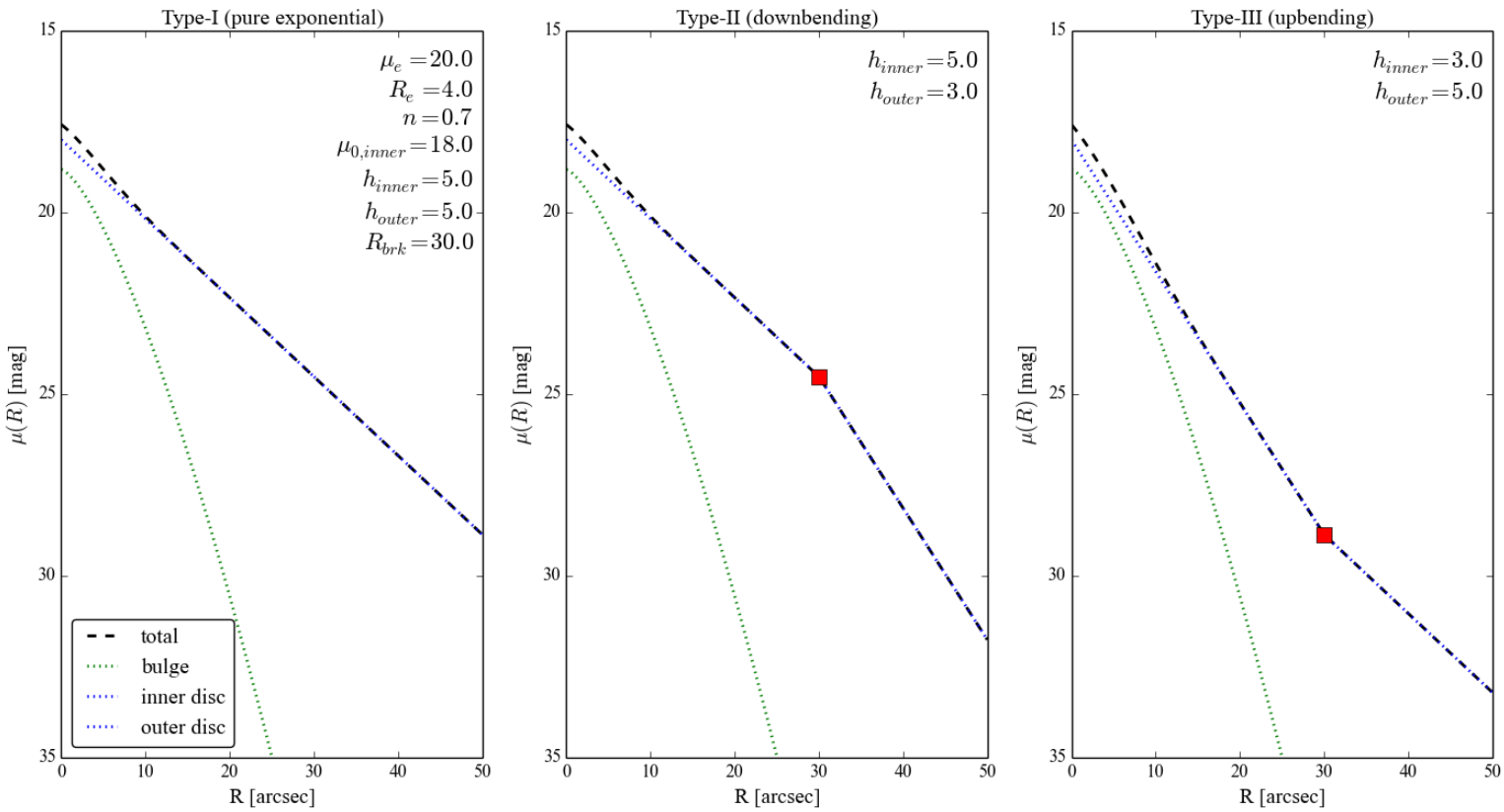

Fig. 4.— The three basic types of truncation with the same bulge parameters. The break radius is indicated as a red box.

While field S0s are divided roughly evenly between all three types, Virgo S0s appear to be completely devoid of type-IIs with $M_v < -17$, $f_{S0} = 0^{+4}_{-0}\%$ (Erwin et al. 2012). Since type-IIIs are found to be equally common in both environments, the difference is made up of type-I profiles, making single-exponentials twice as common in the Virgo cluster than in the field.

To account for such a drastic change in type population, either something in the (early) cluster transforms type-II into type-I or something prevents the opposite transition which is common in the field. Assuming cluster S0s originally had type-II truncated profiles, then a mechanism is required which erases said truncation.

1.6. Aims of Project

In this project, we investigate the feasibility of detecting and classifying truncations in the coma cluster S0s using a simple 1D bulge-disc decomposition procedure.

Erwin et al. (2012) used a sample of 24 S0s within the Virgo cluster. By studying Coma S0s we can select a larger number of S0s over a wide range of cluster-centric radii and hence compare and contrast the results with Erwin et al. (2012).

In addition, we also investigate truncation type as a function of cluster-centric radius in an effort to see if the truncation mechanism also depends on cluster density as well as cluster membership.

Lastly, a search for a correlation between Sérsic parameters and truncation type is investigated.

2. Data and Initial Sample

An initial large sample of 620 galaxies of disk galaxies from Head et al. (2014) in the Coma Cluster was used as a basis for further refinement. Cluster membership was determined by redshift ($z_{coma} = 0.023$), with the centre of Coma taken as the mid-point between NGC4874 and NGC4889.

The i-band was selected in order to avoid the catastrophic OH-brightening and water absorption in the far-infrared and to enhance detection of 'red and dead' S0s. Images were obtained from both SDSS and MegaCam for each galaxy in the sample. A point spread function (PSF) full-width half-maximum (FWHM) of between $0.65''$ and $0.84''$ was typical (Head et al. 2014). The PSF profile was excluded from further analysis by considering only $R > 1$ arcsec. The pixel scale was 0.396 arcsec pix^{-1} for SDSS and 0.186 arcsec pix^{-1} for MegaCam. Zeropoints were pre-calculated but average at ~ 30 mag.

3. Data Reduction and Analysis

3.1. Extracting 1D Profiles

We extract two 1-dimensional profiles for each image. In our implementation, wedges drawn along each direction of the major axis centred by fitted isophote ellipses and the median counts are calculated along the axis at regular intervals (with central counts being

determined by interpolation). The profile is terminated when the counts become consistently lower than the sky value given by SDSS/MegaCam pipeline. This results in four 1D profiles for each galaxy with varying sizes of regions where the sky becomes dominant.

3.2. Sky Subtraction

3.2.1. The effects of sky

The night sky is never completely dark and in the i-band it has a brightness of 19.9 mag arcsec^{-2} (Binney & Merrifield 1998). Indeed, proficient sky subtraction is required for the acquisition of accurate surface brightness profiles at low brightness. If the sky background is underestimated, the sky will contribute to the profile at large galactic radius and flatten off the profile if sufficiently extended. If the background is overestimated, light from the galaxy is subtracted also, plunging it towards zero at some finite radius.

There are, however, other errors that contribute to the overall corruption of the image besides sky estimation. Due to the limitations of optical devices and CCDs, there may be a gradient across an image frame to due to CCD bias or inhomogeneous illumination (Olsen et al. 2010). Joining frames together, or 'splicing' exacerbates this effect since different exposures will have different sky backgrounds. The raw data is already corrected for this by SDSS and MegaCam in flat-fielding corrections, but the correction is not perfect and may result in unwanted artefacts or gradients across the image. SDSS operates in drift scan mode (Abazajian et al. 2009) and so does not suffer as much from the effects of flat-fielding since any bias or aberration is averaged out.

3.2.2. Finding the Sky

Accurate background estimates are essential in characterising outer profiles. While both cameras give their own estimated sky fluxes and the extraction of 1D profiles yields a additional estimate, background can vary within images -and between major axis profiles- due to flat-fielding errors (Bijaoui 1980).

To find the radial position at which the sky starts to dominate, the profile is divided into chunks of three data points. For each chunk, the local mean and standard deviation are calculated. This is essentially finding the local value of intensity. We define the point at which the sky starts to dominate as the point where $\bar{I}_{i+1} > \bar{I}_i + \sigma_i$, where $\bar{I}_i$ is the local mean intensity and σ_i is the standard deviation at point i. We initiate this search from the

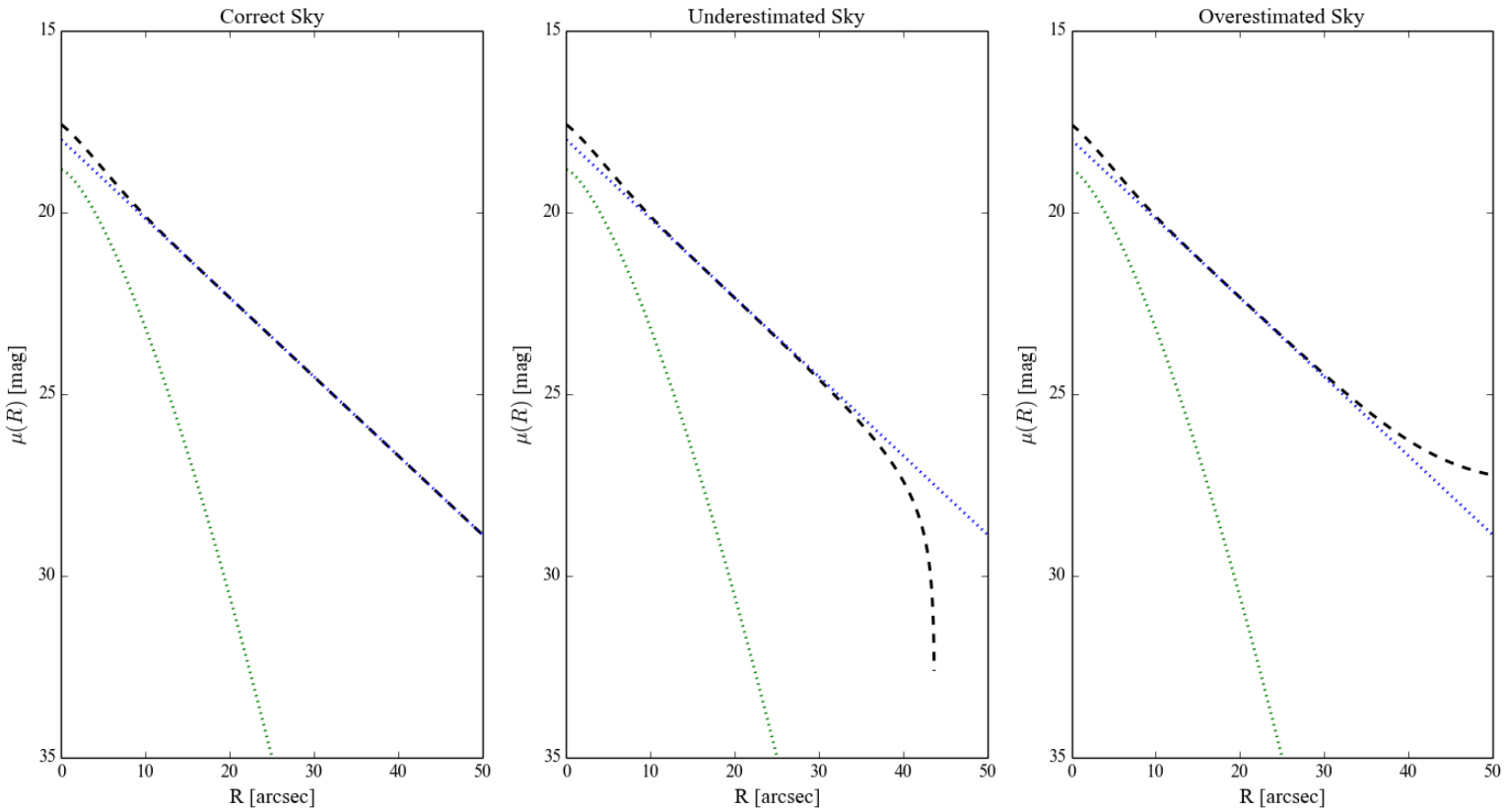

Fig. 5.— The effect of an error in the sky of ±5 counts

end of the profile. The effects of local minima and maxima due to stars and noise are also taken into account by considering the next two local means instead of just one (i.e. $\bar{I}_{i+2}$).

The mode is the best estimate for the sky value since it is the peak of the brightness frequency distribution (Bijaoui 1980). Therefore, we use a 3σ-clipped, synthetic mode to estimate the sky values.

The value for sky uncertainty is calculated by first 'clipping' the sky dominated area so that values that lie further than 3σ away from the mean sky value are removed. We use a similar synthetic mode to Peng et al. (2010) of 3(median) − 2(mean) to calculate sky brightness along with its standard deviation for the sky uncertainty.

We define the critical surface brightness μ_{crit} as the surface brightness up to which the profile is considered reliable. μ_{crit} is placed where we calculate the difference between under and over subtracted profiles (i.e. $\pm 1\sigma_{sky}$) to be 0.2 mag. This is a more useful measurement

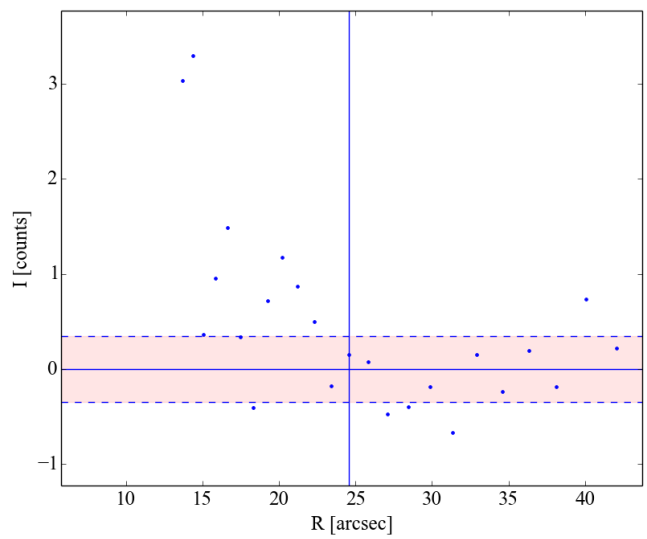

Fig. 6.— Area of the profile from 1237667324334506284 (MegaCam axis 1) with the sky uncertainty shown in red and the cut off point as the vertical straight line

of sky than a $\pm 3\sigma$ since it shows us where the actual profile starts to be affected.

3.3. Bulge-Disc Decomposition

Sérsic parameters for each profile are determined by bulge-disc decomposition. We use the Levenberg-Marquardt non-linear least squares regression algorithm (LMA) to minimise chi-squared and fit the profile to the desired model. Reduced chi-squared is used as a goodness-of-fit measure.

$$\chi^2_\nu = \frac{1}{N-n-1} \sum_i \frac{[y_i - f(x_i)]^2}{w_i^2}, \tag{2}$$

where χ^2_ν is the reduced chi-squared goodness-of-fit measure, N is the number of data points, n is the number of free parameters, y_i are the data points, $f(x_i)$ are the associated model points and w_i are the associated weightings for each point (Marquardt 1963). A reduced chi-squared of $\chi^2_\nu \approx 1$ describes an accurate fit, $\chi^2_\nu < 1$ describes overestimated errors and $\chi^2_\nu > 1$ is degenerate in describing both underestimated errors or an incorrect model. This is by far the most tested and reliable fitting method (Lawson 1995) and was implemented in the high-level language Python with Scipy (Oliphant 2007).

We use an exponential disk + Sérsic $R^{1/n}$ bulge model used in Allen et al. (2006) as bulges cannot all be described by $R^{1/4}$ (Simard et al. 2011). Fitting a model with six

parameters is challenging to accomplish in one fell swoop since there is more parameter space to explore and so the likelihood of being trapped in a local minima -and not a global minima- increases. Therefore, we employ an iterative method similar to that found in Weinzirl et al. (2009) as follows:

1. Sérsic fit:
   A Sérsic bulge (free n_B) is fit to the profile with a radial surface brightness of:
   $$I(R) = I_e \mathrm{exp}\left\{-\mathrm{b_n}\left[\left(\frac{\mathrm{R}}{\mathrm{R_e}}\right)^{1/\mathrm{n}} - 1\right]\right\}, \tag{3}$$
   where we use the definitions given earlier. LMA converges quickly to a solution for a single Sérsic roughly independent of initial parameter guesses.

2. Bulge+disk fit:
   The Sérsic bulge is duplicated and has its Sérsic index n set to unity. The model now reads:
   $$I(R) = I_0 \mathrm{exp}\left\{-\frac{\mathrm{R}}{\mathrm{h}}\right\} + \mathrm{I_e}\mathrm{exp}\left\{-\mathrm{b_n}\left[\left(\frac{\mathrm{R}}{\mathrm{R_e}}\right)^{1/\mathrm{n}} - 1\right]\right\}, \tag{4}$$
   where we now use the disc scale length $h = R_{e,disc}/1.678$ and central intensity $I_0 = I_{e,disc}e^{-1.678}$ instead of $R_{e,disc}$ and $I_{e,disc}$ in order to distinguish concisely between bulge and disc parameters.

Fitting the usual assortment of effective magnitudes, effective radii and Sérsic indices will sometimes result in an Allen Type-4 'inverted' profiles where the bulge dominates at large radii and the disk dominates at the centre (Allen et al. 2006).

Since we have already removed the sky and specified that we reject galaxies whose bulge dominates at large radii, we can assume that these solutions are likely the result of LMA attempting to fit a truncation or some other object such as a foreground star. To avoid these unreal solutions, the bulge+disk system is fit using effective radii difference and bulge-disk ratios (henceforth known as ΔR_e and B/D) instead of the parameters themselves. Limits are placed upon them such that $B/D < 1$ and $\Delta R_e = 1.678h/R_e > 1$, to only permit disk dominated solutions. The bulge to disc ratio is

$$\frac{B}{D} = \frac{n\Gamma(2n)}{b^{2n}}\left(\frac{R_e}{h}\right)^2\left(\frac{I_e}{I_0}\right), \tag{5}$$

where $b = b_{n,bulge}$.

Weights for use in LMA are computed in raw photon counts on a per pixel basis. The total error in intensity for each point is given by

$$\alpha = \frac{1}{s_{pix}^2}\sqrt{\alpha_I^2 + \alpha_{extraction}^2 + \alpha_{sky}^2}, \tag{6}$$

where s_{pix} is the pixel scale, $\alpha_{extraction}$ is the error in forming a 1D profile along the major axis, α_{sky} is the sky uncertainty and α_I is the error in counts given by

$$\frac{\sqrt{I_{phot}G}}{G}, \tag{7}$$

where I_{phot} is the raw photon count and G is the CCD gain.

3.4. Truncation Detection

Fitting a galaxy with an un-truncated model, as above, is helpful to quantify the bulge size. It even gives some measure of truncation type through its residuals.

To quantify a truncated surface brightness profile, three bulge parameters; two sets of scale lengths and central magnitudes; and a break radius are required. We do not fit a truncated model straight to the whole surface brightness profile as this is yet more unstable than the five parameter bulge-disc model due to the additional four parameters needed. We use a method similar to that of Pohlen & Trujillo (2006) whereby we instead, derive the break radius and then fit the truncated disk to the disk dominated area.

We define a disk dominated region where the disk is not more than 0.2 mag away from the total surface brightness and is not smaller than μ_{crit}. This avoids noise from both the sky and the bulge.

The new disk profile is first smoothed using an unweighted B-spline function (Dierckx 1975) of order 3. Then a median-filter is used to remove the last of extreme values with a smoothing length of 10% of the length of the region. The profile is then broken into overlapping chunks of three data points, to which a straight line is fitted. This results in an approximated derivative of the profile and estimate of the local scale length h_{loc} at each point.

Since the transition from scale lengths at the break radius has been found to be frequently smooth (Erwin et al. 2008; Pohlen et al. 2004; Maltby et al. 2011), we assume that there are now two regions of constant scale length joined by a transition region.

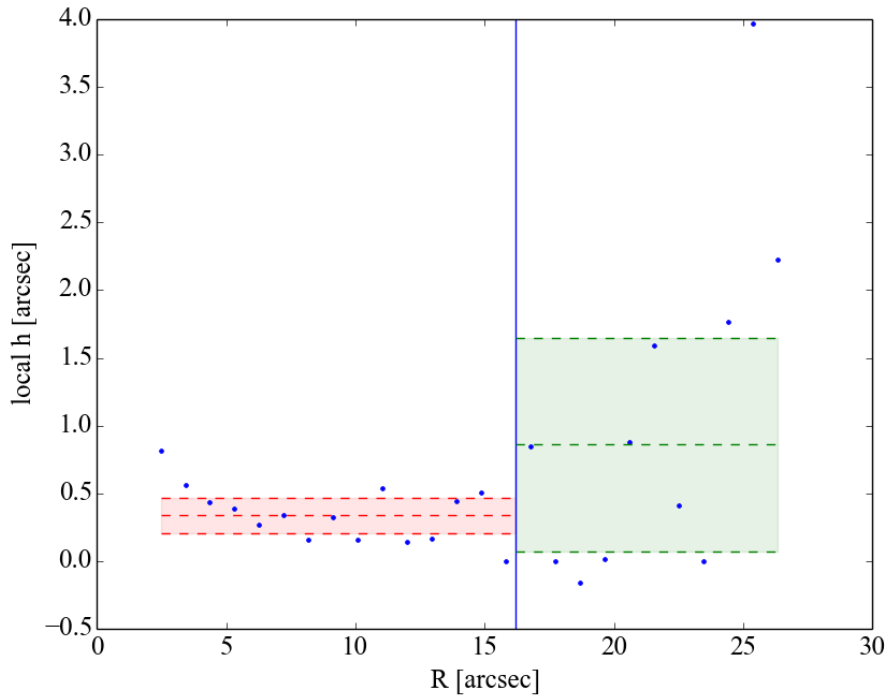

Fig. 7.— Truncation break radius derivation for 1237667324334506284 (MegaCam axis 2). Standard deviations for each side are shown.

We define the boundaries of the transition region as the point where the local scale length - starting from the break radius - reaches a value of 1σ away from the inner and outer means. These boundaries provide a measure for break radius uncertainty.

We then proceed to fit a straight line to the magnitudes of both the inner and outer disk regions. We do not use the intensity counts because the outer disk is usually plagued with negative values and it is less computationally intensive. Due to the fact that the break region may be large, we do not restrict ourselves to not fitting inside it.

We fit the truncated disk using break radius, outer scale length, outer central surface brightness and scale length difference:

$$\mu_{outer} = \mu_{0,outer} + 1.068\frac{R}{h_{outer}} \tag{8}$$

$$\mu_{inner} = \mu_{0,outer} - \Delta\mu + 1.068R\left(\frac{1}{h_{outer}} + \Delta h\right) \tag{9}$$

$$\Delta\mu = 1.086R_{brk}\Delta h = \mu_{outer} - \mu_{inner} \tag{10}$$

$$\Delta h = \frac{1}{h_{inner}} - \frac{1}{h_{outer}}, \tag{11}$$

where μ_{inner} is the surface brightness of the inner disk, μ_0 is the central surface brightness, h is the scale length and R_{brk} is the break radius, which was restricted between the boundaries established during detection.

Classification of three or more such breaks is not uncommon in other works (Pohlen & Trujillo 2006; Gutiérrez et al. 2011) but does lead to complications when trying to find the means around each break radius. In our investigation, it is assumed that there are no more than two break radii and this works well for the majority of cases.

3.5. Parameter Uncertainties

The uncertainties of LMA can be computed from the covariance matrix of a fit (Hughes 2010), but we implement a bootstrapping resampling procedure to estimate the errors on each fit parameter.

We resample our data points, with replacement, and fit 1000 times to get a distribution for each parameter. The standard deviations and means are then calculated from this distribution.

In addition to the errors due to sampling and fitting (measured by bootstrapping), we calculate the error due to sky uncertainty. The profile is adjusted to 200 values within the sky uncertainty and the truncation algorithm is run for each of the new sky brightnesses We use these parameters as confidence intervals for the truncated disk since the limiting factor for characterising the outer disk is the sky level.

4. Results

4.1. Sky Detection

The automated detection routine as describe above successfully finds the sky dominated area with all sample light profiles. The sky value obtained from our detection algorithm differed from the values delivered from the SDSS/MegaCam pipeline by as much as 5%, though typically only differs by about 0.3%. Sky uncertainty as the standard deviation differs from the pipeline uncertainties ($\sqrt{sky}$) by around 40%.

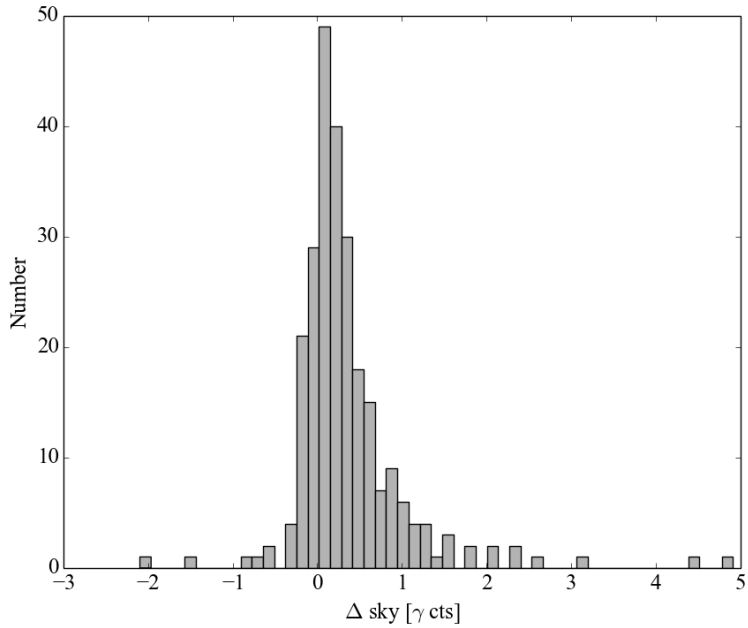

Fig. 8.— Histogram of the differences between our sky values and MegaCam/SDSS

4.2. Example Decomposition

We present a typical galaxy decomposition and classifications for a disk exhibiting up-bending to illustrate the classification process. ID 1237667444048265310 is a typical example of a type-III classified galaxy.

Figure 4.2 shows the surface brightness profile of 1237667444048265310. Both MegaCam profiles, representing the different major axes, are completely independently fit. This galaxy is a typical example of an error in truncation detection. Usually there is one profile per galaxy which exhibits this undesirable behaviour. This problem cannot be remedied by restricting the parameters in the fit, since any more restriction tends to yield unreal solutions such as lack of bulge.

Firstly, a simple bulge + disc is fit to the profile, resulting in a typical profile with a disc scale length of ~ 6 arcsec and bulge effective surface brightness of ~ 20 mag.

On the other hand, the bulge shape -characterised by the Sérsic index- varies between SDSS and MegaCam fits. Though this changes the shape of the bulge entirely, its surface brightness remains small enough ($\mu_B < \mu_D + 0.2$ mag) as to not have an impact the total at large R.

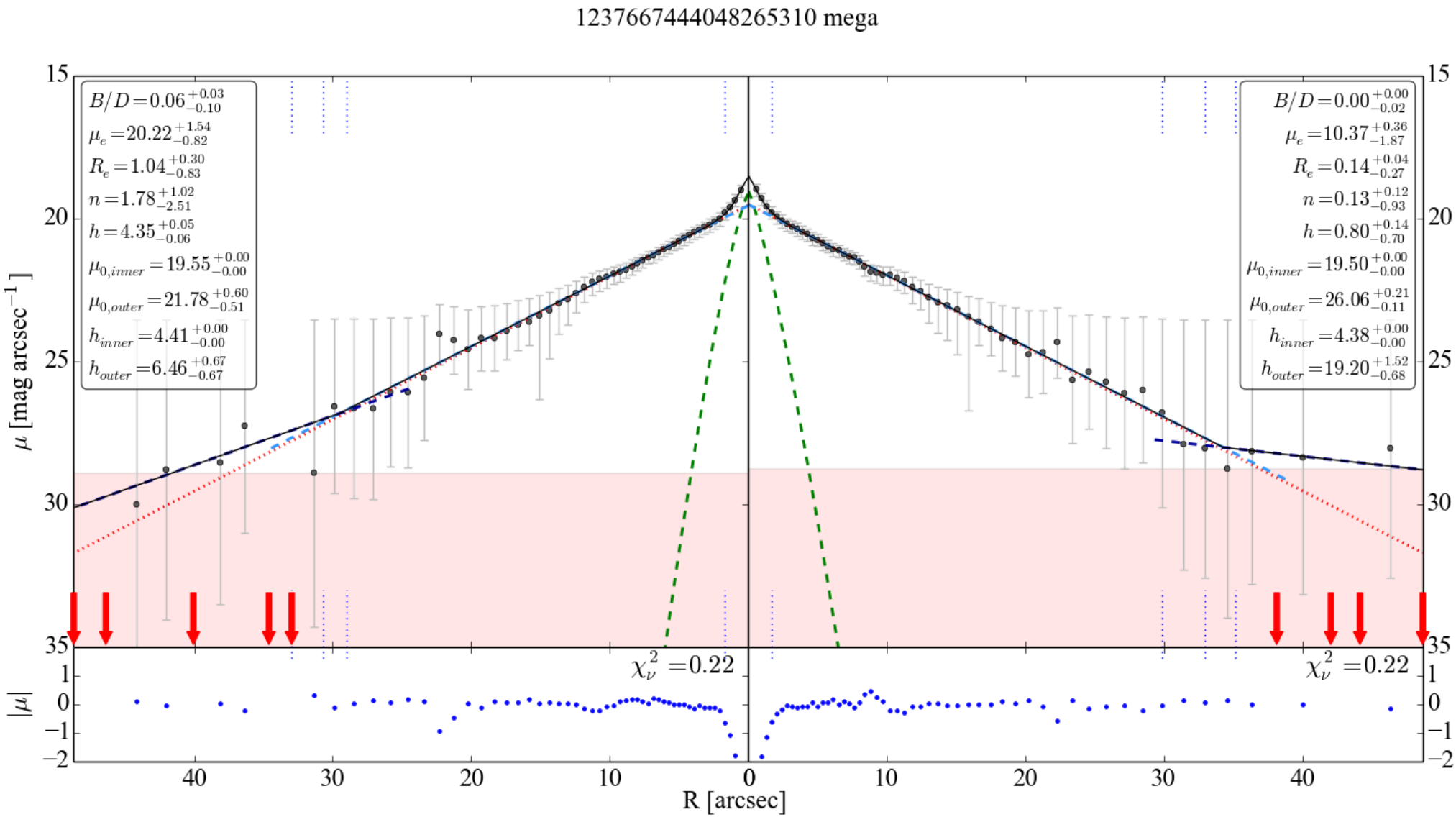

Fig. 9.— The surface brightness profile for the MegaCam image of 1237667444048265310. The plot shows the inner and outer disks in light and dark dashed lines respectively. The bulge is illustrated in green and the original pre-truncated disk is shown as a red dotted line. The total is depicted with a thin black line. Unreal (negative counts) values are shown with red arrows and the critical sky value as the red region. The dashed lines at the top and bottom denote the lower sky limit, lower break limit, upper break limit and bulge cut-off radius, working inwards. Normalised magnitude residuals are shown at the bottom.

Next, the automated truncation detection yields a potential break point and the two disks are parameterised. The routine classifies these individual fits as Type-III (upbended) since the lower limit on the outer scale length does not fall below the upper limit on the inner scale length.

As seen in the residual plot accompanying the fits, there is poor fit at the centre of the galaxy, where the bulge is strongest. Since the truncation fit only subtracts the bulge's contribution to the total magnitude, it is likely that the poor central fit is due to neglection of bulge light.

The next step is to combine the images to yield overall parameters for the entire galaxy. However, although there is a good agreement of pre-truncated-fit -called 'classic' from now on- disk parameters between cameras there is a discrepancy in the Sérsic index of the bulge. SDSS fits a small $n \approx 0.5$ bulge whilst MegaCam finds an expansive $n \approx 1.5$ bulge.

This discrepancy error is a major problem when combining results as averaging the parameters does not yield an accurate 'one-size-fits-all' solution. The truncation is commonly classified differently between cameras. We proceed by combining their bootstraps instead. This does not solve the problem of not yielding an accurate solution but it does provide an accurate error on the result, unlike a weighted arithmetic mean (Andrae 2010).

Defining the truncation strength as

$$S_h = \frac{h_{outer} - h_{inner}}{h_{inner}}, \tag{12}$$

we find that $S_h = 1.3^{+0.9}_{-0.7} > 0$ for the combined profile and so is classified as Type-III.

4.3. Sample Properties

Though all profiles have been successfully fit with a disk dominated outer profile, it was not always real. There were frequent situations where a disc with perturbation (Allen type-6) were fit. These galaxies usually had what appears to be previously unseen spiral patterns, wide bars or simply a bulge dominated outer profile. Since these components are not part of this investigation, these galaxies were discarded.

We restricted ourselves to using galaxies with inclination (axis ratio) $b/a > 0.4$ and bulge size $R_{e,bulge} < 0.2R_{e,disk}$. This removed a great many bulge dominated systems, shrinking our sample to 83 galaxies. The initial sample of profiles was also filtered by removing galaxies whose profiles yield hugely disagreeing results. This was done by eye and the sample was refined to 66 reasonable fits.

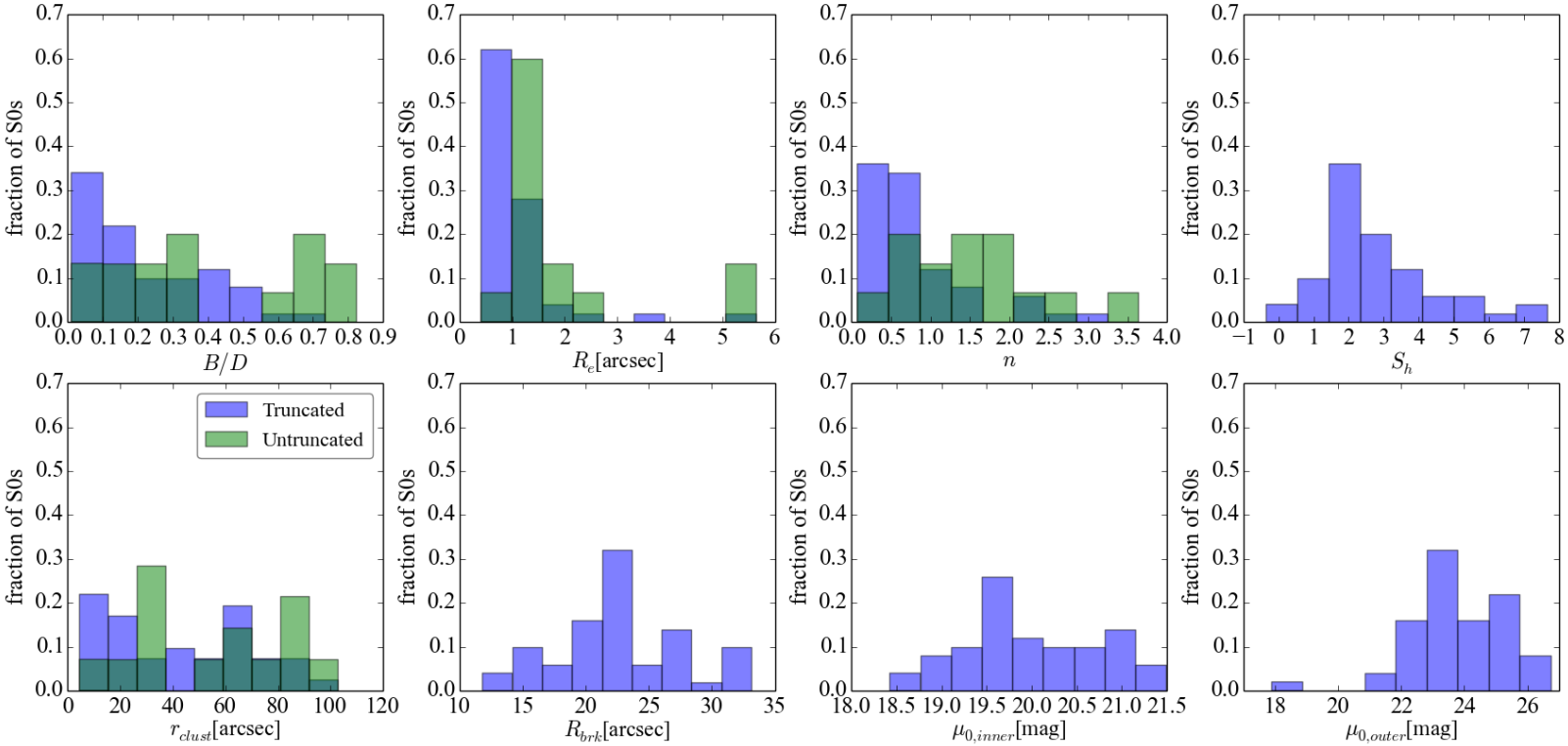

Fig. 10.— Proportion of both truncated and untruncated disks as a function of various parameters where available

Our sample exhibits a range of bulge sizes, showing that our restrictions on bulge parameters relative to the disk has had little impact on the diversity of our sample. With a typical bulge of $R_e = 1.0 \pm 0.9$ arcsec and $n = 0.8 \pm 0.7$, the bulge clearly tends to be less luminous that the disk in truncated systems and more centrally concentrated than in type-Is ($R_e = 2 \pm 1$ arsec and $n = 1.5 \pm 0.9$). The type-III preference for a more centralised bulge suggests that the upbending is not due to bulge influence at large R, which earlier, may have escaped notice.

In Type-III disks, the central surface brightness of the outer disk must be greater than that of the inner disk. This can clearly be seen in the sharp divide between the distributions in figure 10. The typical inner central surface brightness is 20.0 ± 0.8 mag whereas in the outer disk it spans a wider range of values with a higher mean 24 ± 2 mag.

In truncated galaxies, the break point takes a wide range of radii and the strength of the break exhibits a peak at 2. The small number of truncated galaxies with low break strength can be attributed to the classification process, since a low break strength is more likely to lie within $\sim 1\sigma$ of the classical disk and hence classified as untruncated.

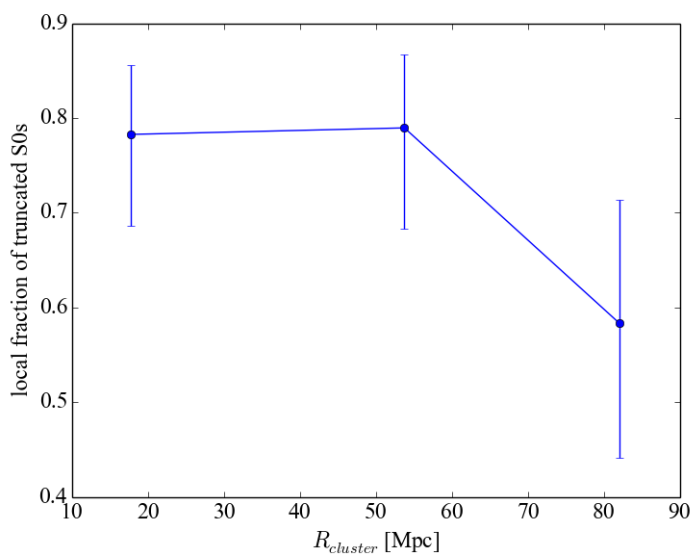

Fig. 11.— Fraction of upbended S0s binned with equal distance bins. Error bars show 68% confidence intervals (Wilson 1927)

We find that 74^{+5}_{-5}% of S0s in the Coma cluster are anti-truncated type-IIIs and a corresponding 24^{+6}_{-5}% are untruncated. The remaining 2% of type-IIs consist of one galaxy (see Discussion for further information).

4.4. Correlations

We found no statistically significant evidence of a trend between distance from cluster centre and bulge and classical disk parameters . However, there is a parabolic region of $30 \lesssim R_{clust} \lesssim 60$ arcsecs, $28 \lesssim \mu_{0,outer} \lesssim 25$ mag in which there are no truncated galaxies.

There is a slight trend for truncated galaxies to be found at lower cluster radii seen in figure 10 but this is not statistically significant.

We found evidence of a weak trend between the bulge magnitude and the break radius. A Pearson correlation coefficient of 0.26 indicates an increase in bulge magnitude as the break appears further out in R. Type-I S0s exhibit a tighter correlation between their potential

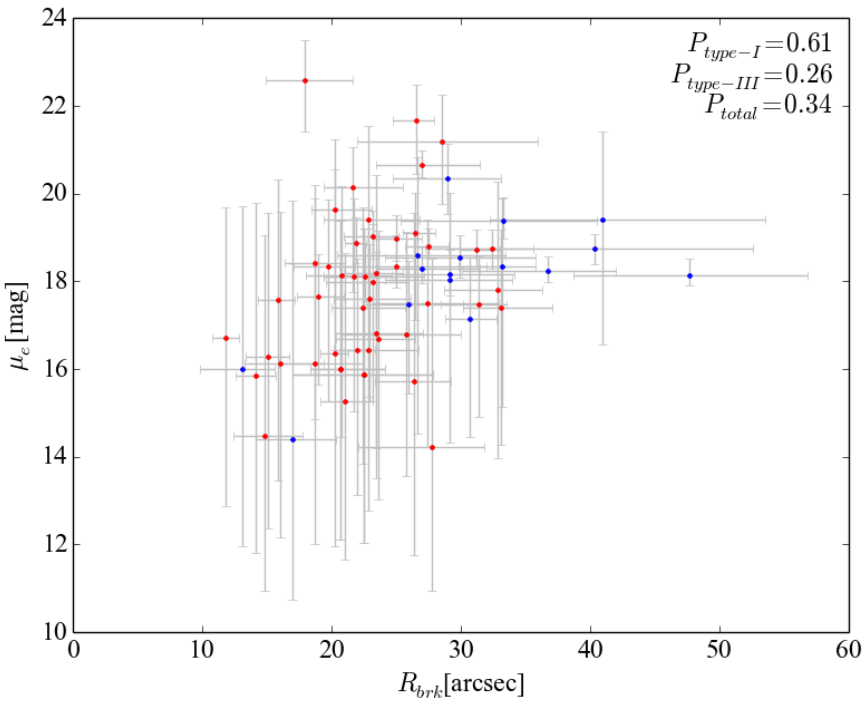

Fig. 12.— A correlation plot between effective bulge magnitude μ_e and break radius R_{brk} with truncated galaxies shown in red and untruncated galaxies shown in blue for comparison.

break radius and bulge magnitude. This demonstrates that this trend is likely an artefact of the fitting process.

A weak trend in fraction of type-III against cluster-centric radius is observed when binning the galaxies into inner, outer and intermediate radii (see figure 11). The fraction of truncated S0s at the outskirts ($R > 60$Mpc) is much lower than that of the innermost

region.

5. Discussion

We have developed techniques for automated sky analysis, bulge+disc fitting and truncation characterisation. We have compiled truncation parameters for a large sample of galaxies and investigated their correlations cluster environment.

Figure 10 shows that truncated galaxies have a wider range of effective bulge magnitudes with smaller Sérsic indices. This suggests that truncated galaxies have a more concentrated brighter centre consistent with the hypothesis of formation by galaxy harassment whereby the centre receives gas from the outskirts (Moore et al. 1996).

There is one type-II in our study, making up just under 2% of our sample. This is consistent with the findings of Erwin et al. (2012) in that there are very few if any disks which exhibit downbending in the cluster environment.

However, our study finds that there is a greater divide between Type-Is and Type-IIIs with 24% and 74% respectively. Referring to the findings of Erwin et al. (2012) in figure 13, the frequency of type-I S0s appears not to be dependent on environment. This implies that the difference between field and cluster type-II fraction is made up of type-III. This strongly suggests that type-Is form by the same path in both the field and cluster environments with the other two types evolving by a different mechanisms. For this to be true requires that either type-IIs are not generated in the cluster at all, or they undergo a massive increase in outer disk brightness or simply that many more type-IIIs are created.

The model galaxy found in Moore et al. (1999, 1996) was transformed from a classical type-I disk to one with a mild anti-truncation by way of galaxy harassment. Given the mildness of the upbending, it is unlikely that process can transform from type-II to type-III. The creation of type-IIs is therefore presumably suppressed at all times during cluster evolution or so slow compared to the anti-truncation rate that the distribution at $z = 0$ contains little downbending disks.

Given that Virgo and Coma are at roughly the same close redshift ($z = 0.03, 0.02$ respectively) (Bower et al. 1992) and that the cluster sample in Erwin et al. (2012) is under half the size of this study, it is possible that with a larger sample, Virgo may exhibit the same relation as found here.

The weak trend in figure 11 could indicate that there is an increase in type-IIIs with decreasing cluster-centric distance, but more data is required to resolve the trend. If there is

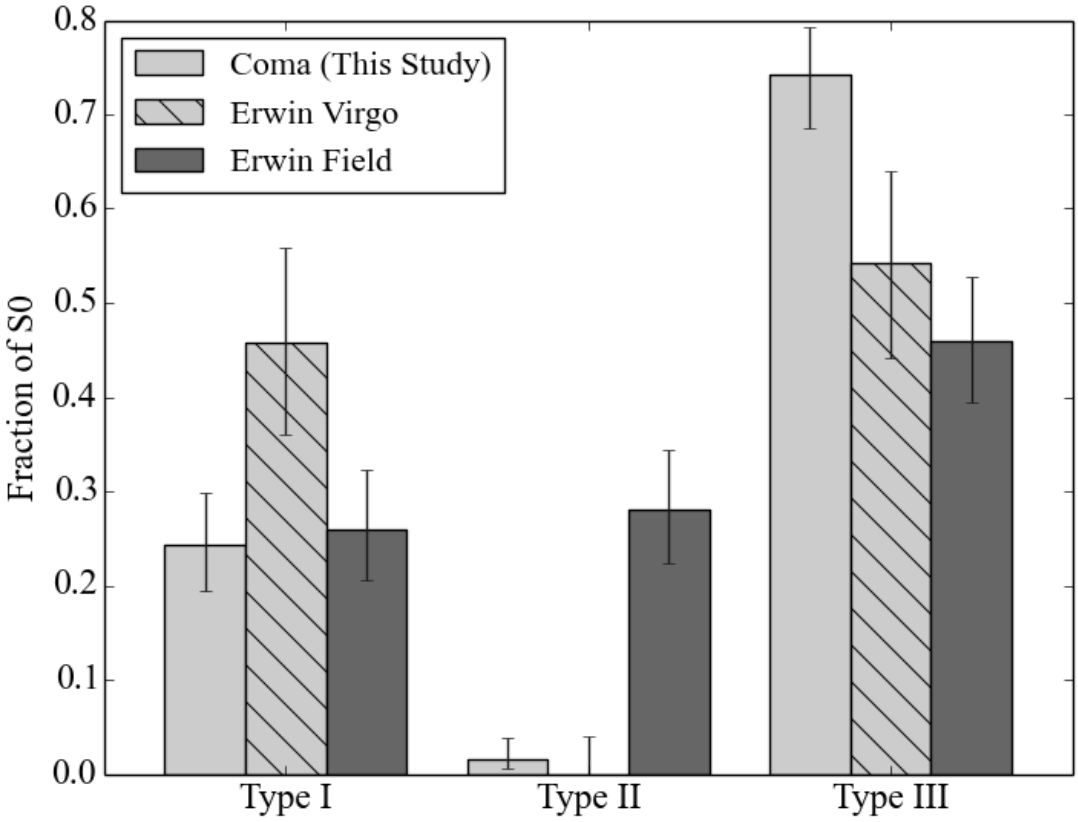

Fig. 13.— Comparison of Type fraction in the Coma cluster to the Virgo Cluster and the field (Erwin et al. 2012). Error bars show 68% confidence intervals (Wilson 1927)

indeed a correlation between radius and frequency of type-IIIs, this would strongly suggest that their formation mechanism is galaxy interaction based. It is currently equally, if not more, probable that there is no trend within the cluster itself.

5.1. Problems with this method

Fitting in 1D is swift and easier than a full 2D decomposition. However, neglecting most of the light of the galaxy impacts on the accuracy of the profile fitted. Any perturbation or artefact -such as a bar or flat-fielding error- included in the major axis wedge cannot be easily or safely removed. Therefore, the two major axis profiles will strongly disagree if there is a slight difference between them (see 4.2). Further problems arise from the combination

of profiles from different cameras.

Combining four bootstraps is effective when the individual results are already close to each other (within $\sim 1\sigma$) and a disagreeing fourth may be discarded provided the other three agree. When there is a divide in parameter space larger than $\sim 2\sigma$ the resulting combination will yield a result which neither bootstrap group supports and with large errors.

Sky detection has worked effectively in this investigation but whether our values are correct or not is untestable until there are more readings around the galaxy in addition to those at the end of the major-axis.

Although the truncation detection algorithm will find a potential break radius, to tends to assign these to high R on some galaxies. This yields scale lengths of 20 arcsec and above, which are unreasonable. The residuals from the fit at low R are also found to be high due to the neglection of bulge light. To fix these problems, we propose that the truncation should be characterised by a full profile fit (including the bulge and sky dominated region) after a break radius region is identified.

6. Conclusion

We have used SDSS and MegaCam i-band images to investigate truncations in S0s present in the Coma Cluster. Using a refined sample of 66 galaxies exhibiting a wide range of bulge and classical disk parameters, we have taken two 1D profiles along the the major axis for each image. The resulting four profiles were first fit with a Sérsic bulge + exponential disk model with the requirement that disk dominates at large R. Then the truncation point was found and a truncated disk fit yielding a distribution of truncated, anti-truncated and classical exponential disks. The four profiles for each galaxy are then combined with their bootstrapped confidence intervals to give overall parameters for the galaxy.

Our main conclusions are:

- 1D decomposition with truncation can be easily automated and requires little computational effort. The iterative sky finding algorithm is also effective at measuring mean sky levels at large R.
- There is a tendency for this procedure to place break radii towards the end of the profile i.e. where the sky starts to dominate. This needs to be corrected by a full component fit over the whole profile.
- We find strong evidence for the suppression of formation of type-II truncated galaxies

in the cluster environment, in agreement with values found in the Virgo cluster (Erwin et al. 2012)

- We find that type-III anti-truncated disks are significantly more frequent than type-I single exponential disks in the cluster.
- We measure that type-Is are equally frequent in both field and cluster environments. This suggests that the formation of type-IIs is heavily suppressed compared to type-IIIs.
- We observe brighter and more centrally compact bulges in type-IIIs than type-Is and conclude that this supports the galaxy harassment hypothesis of type-III formation
- We measure a weak trend of increasing type-III fraction with decreasing cluster-centric radius suggesting that type-IIIs form more frequently in high density environments

Although it is possible to characterise truncations with this method, there is significant error combining four profiles. A 2D fit and decomposition would undoubtedly render more robust and accurate results.

REFERENCES

Abazajian K. N., Adelman-McCarthy J. K., Agüeros M. A., Prieto C. A., 2009, ApJS, 182, 543

Allen P. D., Driver S. P., Graham A. W., Cameron E., Liske J., Propris R. D., 2006, MNRAS, 371, 2

Andrae R., 2010, ARXIV

Bedregal A. G., Aragón-Salamanca A., Merrifield M. R., 2006, MNRAS, 373, 1125–1140

Bekki K., 1998, ApJL, 502, L133

Berendzen R., Hart R., Seeley D., 1976, NSF, -1

Bijaoui A., 1980, A&A, 84, 81

Binney J., 1998, Galactic astronomy. Princeton series in astrophysics, Princeton University Press, Princeton, NJ

Binney J., Merrifield M., 1998, Galactic astronomy. Princeton University Press, Princeton, NJ

Blanton M. R., Moustakas J., 2009, ARAA

Bower R. G., Lucey J. R., Ellis R. S., 1992, MNRAS, 254, 601

Burstein D., Ho L. C., Huchra J. P., Macri L. M., 2005, ApJ, 621, 246

Carroll B. W., Ostlie D. A., 2007, An introduction to modern astrophysics. Pearson Addison-Wesley, San Francisco

Coles P., 2002, Cosmology: the origin and evolution of cosmic structure, 2nd ed edn. John Wiley, Chichester, Eng

Cortesi A., Merrifield M. R., Coccato L., Arnaboldi M., Gerhard O., Bamford S., Napolitano N. R., Romanowsky A. J., Douglas N. G., Kuijken K., Capaccioli M., Freeman K. C., Saha K., Chies-Santos A. L., 2013, MNRAS

Crocker A. F., Bureau M., Young L. M., Combes F., 2011, MNRAS, 410, 1197

de Vaucouleurs G., 1963, ApJS, 8, 31

DeGraaff R. B., Blakeslee J. P., Meurer G. R., Putman M. E., 2007, ApJ, 671, 1624

Dierckx P., 1975, Curve and surface splitting with splines. Clarendon Press, Oxford; New York

Dressler A., 1980, ApJ, 236, 351

Dressler A., Augustus Oemler J., Couch W. J., Smail I., Ellis R. S., Barger A., Butcher H., Poggianti B. M., Sharples R. M., 1997, ApJ, 490, 577

Dressler A., Sandage A., 1983, ApJ, 265, 664

Erwin P., Beckman J. E., Pohlen M., 2005, ApJL, 626, L81

Erwin P., Gutierrez L., Beckman J. E., 2012, ApJ, 744, L11

Erwin P., Pohlen M., Beckman J. E., 2008, AJ, 135, 20

Freeman K. C., 1970, ApJ, 160, 811

Graham A. W., Driver S. P., 2005, PASA

Gunn J. E., Gott J. Richard I., 1972, ApJ, 176, 1

Gutiérrez L., Erwin P., Aladro R., Beckman J. E., 2011, AJ, 142, 145

Head J. T. C. G., Lucey J. R., Hudson M. J., Smith R. J., 2014, MNRAS

Hubble E., 1926, ADS, 324, 1

Hughes I., 2010, Measurements and their uncertainties: a practical guide to modern error analysis. New York : Oxford University Press, Oxford

Kennicutt J., 1998, ARAA, 36, 189

Kormendy J., Drory N., Bender R., Cornell M. E., 2010, ApJ, 723, 54

Laurikainen E., Salo H., Buta R., 2005, MNRAS, 362, 1319

Lawson C. L., 1995, Solving least squares problems. No. 15 in Classics in applied mathematics, SIAM, Philadelphia

Liddle A. R., 2003, An introduction to modern cosmology, 2nd ed edn. Wiley, Chichester ; Hoboken, NJ

Maltby D. T., Hoyos C., Gray M. E., Aragón-Salamanca A., Wolf C., 2011, MNRAS

Marquardt D. W., 1963, JSIAM, 11, 431

Moore B., Katz N., Lake G., Dressler A., Oemler A., 1996, Nature, 379, 613

Moore B., Lake G., Quinn T., Stadel J., 1999, Monthly Notices of the Royal Astronomical Society, 304, 465

Naim A., Lahav O., Sodre L. J., Storrie-Lombardi M. C., 1995, MNRAS, 275, 567

Oliphant T. E., 2007, CS&E, 9, 10

Olsen D., Dou C., Zhang X., Hu L., Kim H., Hildum E., 2010, Remote Sensing, 2, 464

Peng C. Y., Ho L. C., Impey C. D., Rix H.-W., 2002, AJ, 124, 266

Peng C. Y., Ho L. C., Impey C. D., Rix H.-W., 2010, AJ, 139, 2097

Pizagno J., Prada F., Weinberg D. H., Rix H.-W., Pogge R. W., Grebel E. K., Harbeck D., Blanton M., Brinkmann J., Gunn J. E., 2007, AJ, 134, 945

Pohlen M., Beckman J. E., Huettemeister S., Knapen J. H., Erwin P., Dettmar R.-J., 2004, ADS

Pohlen M., Lütticke R., Dettmar R.-J., 2001 Vol. 230, Cut-off radii of galactic disks. pp 135–136

Pohlen M., Trujillo I., 2006, A&A, 454, 759

Rawle T. D., Lucey J. R., Smith R. J., Head J. T. C. G., 2013, MNRAS

Sersic J. L., 1968, Cordoba, Argentina: Observatorio Astronomico, 1968, -1

Silk J., Nusser A., 2010, ApJ, 725, 556

Simard L., Mendel J. T., Patton D. R., Ellison S. L., McConnachie A. W., 2011, A&A

Sparke L. S., 2000, Galaxies in the universe: an introduction. Cambridge University Press, New York

Tully R. B., Fisher J. R., 1977, A&A, 54, 661

van der Kruit P. C., 1979, A&AS, 38, 15

Weinzirl T., Jogee S., Khochfar S., Burkert A., Kormendy J., 2009, ApJ, 696, 411

Wilson E. B., 1927, JASA, 22, 209

This preprint was prepared with the AAS LaTeX macros v5.2.